

Complex eigenenergy of GDR for ^{16}O by the Jost function within RPA framework

K. Mizuyama^{1,2}, N. Nhu Le^{3,4}, T. V. Nhan Hao^{3,4}, N. Hoang Tung⁵, and T. Dieu Thuy^{3*}

¹ *Institute of Research and Development, Duy Tan University, Da Nang 550000, Vietnam*

² *Faculty of Natural Sciences, Duy Tan University, Da Nang 550000, Vietnam*

³ *Faculty of Physics, University of Education, Hue University, 34 Le Loi Street, Hue City, Vietnam*

⁴ *Center for Theoretical and Computational Physics, College of Education, Hue University, 34 Le Loi Street, Hue City, Vietnam*

⁵ *Faculty of Physics, The University of Danang, University of Science and Education, Da Nang 550000, Vietnam*

(Dated: December 6, 2022)

The Jost function method is extended within the framework of the RPA theory to find poles on the complex energy plane that exhibit complex RPA eigenenergies. Poles corresponding to the RPA excited states such as the giant resonance of ^{16}O electric dipole excitations were successfully found on the complex energy plane. Although the giant resonance has been known as a single resonance with large strength and width, it is found that, at least within the RPA framework, the ^{16}O electric dipole giant resonance is formed by multiple poles, each of which is an independent pole with different widths, origins, response properties to residual interactions, and components structures of the density fluctuation..

I. INTRODUCTION

In nuclear physics, the giant resonance is known as a resonance with a very broad and large strength that appears in the relatively higher continuum energy region above threshold in the cross section or strength function expressed as a function of the excitation energy [1–4]. The random-phase-approximation (RPA) [5] is a powerful tool for the description of the collective excitation of nuclei, such as a giant resonance [6, 7]. Based on the understanding of the schematic model of RPA [8], the RPA solution that is formed by the superposition of a large number of p - h excited configurations and gives a large strength due to the effect of residual interactions is interpreted as a collective excitation mode, and the giant resonance is considered to be such a collective excitation mode.

There are two main methods for solving the equation in RPA theory: one that uses a discrete basis and diagonalises the RPA Hamiltonian to obtain a solution, and the continuum RPA (cRPA) [9] that takes into account the boundary conditions of the continuum. In the former method, all RPA solutions are obtained as discrete energy eigenstates, with giant resonances appearing either as solutions giving large strength at the resonance energy or as many spread discrete solutions near the resonance energy. The width is often evaluated from the empirical reproducibility of the experimental data using the Lorentz distribution function, assuming that the giant resonance has a peak structure with a single width. Since the latter method (the cRPA method) takes into account the boundary conditions of the continuum, it can represent the behavior of the strength function as a smooth function of energy above threshold. Without the assumption of a Lorentz distribution, as a result of numerical calculations, the giant resonance is also represented as a smooth function of energy, which has a peak structure with a width. However, the cRPA method is not able to calculate the width itself.

There is a phenomenological model that describes the width

of the giant resonance in terms of mass number and dissipative term. It is well known that the mass number dependence of experimental values of the giant resonance width estimated by the Lorentz distribution function roughly follows this phenomenological model [10, 11]. This phenomenological model is derived from the Euler equations plus a dissipation term representing viscosity, assuming that the giant resonance is a harmonic oscillation with damping due to viscosity. In calculations such as the second RPA, which include higher-order effects, the discrete strength (of resonances such as the giant resonance) obtained from calculations using a discrete basis is fragmented and spread in energy by the higher-order effects. This spreading of the strength is interpreted as the broadening of the width of the resonance due to higher-order effects (spreading width), however, this is not an argument made by directly calculating the width. [4]. Despite the fact that width is one of the most important characters in the giant resonance, there is still no method that can calculate the width of resonances obtained as the complex eigenenergy states of the nucleus within the microscopic theoretical framework such as the RPA theory.

The Jost function is a function that gives the energy eigenvalues of the fundamental differential equations of a quantum system based on the Hamiltonian of a system such as the Schrödinger equation as zeros on the complex energy plane. The Jost function is given in differential and integral forms, and its differential form is equivalent to the Wronskian. The energy eigenvalues given by the zeros on the complex energy plane give not only bound states but also resonance states. The imaginary part of the zeros on the complex energy plane of the Jost function gives the width of the resonance. However, the original Jost function [12] did not take into account channel coupling (Note that the term “channel coupling” here includes a wide range of meanings, such as the coupling between p - h configurations). In order to apply the Jost function to solve various physics problems, it is necessary to extend the Jost function to be able to consider coupled channels. As a first step, we have extended the Jost function to the Hartree-Fock-Bogoliubov theory framework in Refs.[13–15].

In this paper, we extend the Jost function method within the framework of RPA theory in order to enable the Jost function

* corresponding author: tthuy1406@gmail.com

conditions at $r = 0$ given by

$$\lim_{r \rightarrow 0} \vec{\phi}^{(r1;q\alpha)} = \begin{pmatrix} 0 \\ \vdots \\ 0 \\ \phi_\alpha^{(q)} \rightarrow \begin{pmatrix} r j_{l_\alpha}^{(q)}(k_{1,\alpha}^{(q)} r) \\ 0 \end{pmatrix} \\ 0 \\ \vdots \\ 0 \end{pmatrix} \quad (20)$$

The boundary conditions for the regular solutions $\vec{\phi}^{(r2;q\alpha)}$ (for $\alpha \in (1, \dots, N_q)$ and $q = n$ and p) are given by

$$\lim_{r \rightarrow 0} \vec{\phi}^{(r2;q\alpha)} = \begin{pmatrix} 0 \\ \vdots \\ 0 \\ \phi_\alpha^{(q)} \rightarrow \begin{pmatrix} 0 \\ r j_{l_\alpha}^{(q)}(k_{2,\alpha}^{(q)} r) \end{pmatrix} \\ 0 \\ \vdots \\ 0 \end{pmatrix}, \quad (21)$$

$\vec{\phi}^{(r2;q\alpha)}$ corresponds to the negative energy solution of $\vec{\phi}^{(r1;q\alpha)}$ because there is a relation between $k_{1,\alpha}^{(q)}$ and $k_{2,\alpha}^{(q)}$ as $k_{2,\alpha}^{(q)}(\omega) = k_{1,\alpha}^{(q)}(-\omega)$.

The outgoing boundary conditions at the limit $r \rightarrow \infty$ for the irregular solutions $\vec{\phi}^{(\pm 1;q\alpha)}$ and $\vec{\phi}^{(\pm 2;q\alpha)}$ are given by

$$\lim_{r \rightarrow \infty} \vec{\phi}^{(\pm 1;q\alpha)} = \begin{pmatrix} 0 \\ \vdots \\ 0 \\ \phi_\alpha^{(q)} \rightarrow \begin{pmatrix} r h_{l_\alpha}^{(\pm)}(k_{1,\alpha}^{(q)} r) \\ 0 \end{pmatrix} \\ 0 \\ \vdots \\ 0 \end{pmatrix}, \quad (22)$$

and

$$\lim_{r \rightarrow \infty} \vec{\phi}^{(\pm 2;q\alpha)} = \begin{pmatrix} 0 \\ \vdots \\ 0 \\ \phi_\alpha^{(q)} \rightarrow \begin{pmatrix} 0 \\ r h_{l_\alpha}^{(\pm)}(k_{2,\alpha}^{(q)} r) \end{pmatrix} \\ 0 \\ \vdots \\ 0 \end{pmatrix}, \quad (23)$$

respectively, where $h_l^{(\pm)}$ is the spherical Hankel function defined by $h_l^{(\pm)}(kr) = j_l(kr) \pm in_l(kr)$.

We can define the regular and irregular solution matrix $\Phi^{(r)}$ and $\Phi^{(\pm)}$ using the regular and irregular solutions as

$$\Phi^{(r)} = \begin{pmatrix} \vec{\phi}^{(r1;n1)} & \vec{\phi}^{(r2;n1)} & \dots & \vec{\phi}^{(r1;pN_p)} & \vec{\phi}^{(r2;pN_p)} \end{pmatrix} \quad (24)$$

and

$$\Phi^{(\pm)} = \begin{pmatrix} \vec{\phi}^{(\pm 1;n1)} & \vec{\phi}^{(\pm 2;n1)} & \dots & \vec{\phi}^{(\pm 1;pN_p)} & \vec{\phi}^{(\pm 2;pN_p)} \end{pmatrix}. \quad (25)$$

These matrices are given as the $2(N_n + N_p) \times 2(N_n + N_p)$ matrix which satisfy

$$\left[\frac{\hbar^2}{2m} \mathcal{K}^2 - \left\{ -\frac{\hbar^2}{2m} \frac{\partial^2}{\partial r^2} \mathbf{1} + \mathcal{U} + \mathcal{V} \right\} \right] \Phi^{(r)} = \mathbf{0} \quad (26)$$

and

$$\left[\frac{\hbar^2}{2m} \mathcal{K}^2 - \left\{ -\frac{\hbar^2}{2m} \frac{\partial^2}{\partial r^2} \mathbf{1} + \mathcal{U} + \mathcal{V} \right\} \right] \Phi^{(\pm)} = \mathbf{0} \quad (27)$$

respectively.

The Jost function $\mathcal{J}^{(\pm)}$ is defined as the coefficient matrix which connects $\Phi^{(r)}$ and $\Phi^{(\pm)}$ as

$$\Phi^{(r)\top} = \frac{1}{2} \left[\mathcal{J}^{(+)} \Phi^{(-)\top} + \mathcal{J}^{(-)} \Phi^{(+)\top} \right]. \quad (28)$$

The Wronskian $\mathcal{W}^{(\pm)}$ is defined by

$$\mathcal{W}^{(\pm)} = \frac{\hbar^2}{2m} \left[\Phi^{(r)\top} \left(\frac{\partial}{\partial r} \Phi^{(\pm)} \right) - \left(\frac{\partial}{\partial r} \Phi^{(r)\top} \right) \Phi^{(\pm)} \right], \quad (29)$$

and it is very easy to confirm that this definition of Wronskian is constant for the radial coordinate r , i.e. $\frac{\partial}{\partial r} \mathcal{W}^{(\pm)} = 0$.

By inserting Eq.(28) into Eq.(29) and taking the limit $r \rightarrow \infty$, it is very easy to obtain the relation formula between the Jost function and Wronskian given by

$$\mathcal{J}^{(\pm)} = \pm \frac{2m}{i\hbar^2} \mathcal{W}^{(\pm)} \mathcal{K}. \quad (30)$$

Applying the Green's theorem to Eq.(26), we can obtain

$$\begin{aligned} & \left[\chi^{(\pm)\top}(r) \frac{\partial}{\partial r} \Phi^{(r)}(r) - \left(\frac{\partial}{\partial r} \chi^{(\pm)\top}(r) \right) \Phi^{(r)}(r) \right] \pm i\mathcal{K}^{-1} \\ &= \frac{2m}{\hbar^2} \int_0^r dr' \chi^{(\pm)\top}(r') [\mathcal{U}(r') + \mathcal{V}(r')] \Phi^{(r)}(r') \end{aligned} \quad (31)$$

where $\chi^{(\pm)}$ is the free particle wave function matrix which satisfies

$$\left[\frac{\hbar^2}{2m} \mathcal{K}^2 + \frac{\hbar^2}{2m} \frac{\partial^2}{\partial r^2} \mathbf{1} \right] \chi^{(\pm)} = \mathbf{0} \quad (32)$$

and the components are represented by the spherical Hankel function.

By inserting Eq.(28) into Eq.(31) and taking the limit $r \rightarrow \infty$, we can obtain the integral form of the Jost function

$$\begin{aligned} \mathcal{J}^{(\pm)\top} &= \mathbf{1} \mp \frac{2m}{\hbar^2} \frac{1}{i} \mathcal{K} \int_0^\infty dr' \chi^{(\pm)\top}(r') \\ &\quad \times [\mathcal{U}(r') + \mathcal{V}(r')] \Phi^{(r)}(r'). \end{aligned} \quad (33)$$

B. Perturbed Green function and RPA response function

The Green's function is defined as a function which satisfies

$$\left[\frac{\hbar^2}{2m} \mathcal{K}^2 - \left\{ -\frac{\hbar^2}{2m} \frac{\partial^2}{\partial r^2} \mathbf{1} + \mathbf{U} + \mathbf{V} \right\} \right] \mathcal{G}^{(\pm)}(r, r') = \mathbf{1} \delta(r - r'). \quad (34)$$

can be represented as

$$\mathcal{G}^{(\pm)}(r, r') = \theta(r - r') \Phi^{(\pm)}(r) \left(\mathcal{W}^{(\pm)-1} \right) \Phi^{(\pm)\top}(r') + \theta(r' - r) \Phi^{(\pm)}(r') \left(\mathcal{W}^{(\pm)-1} \right)^\top \Phi^{(\pm)\top}(r) \quad (35)$$

by using the Wronskian. Note that this Green function is also given in the form of $2(N_n + N_p) \times 2(N_n + N_p)$ matrix (The proof of Eq.(35) is shown in Appendix. 1).

The RPA equation when the external field exists is given by

$$\left[\frac{\hbar^2}{2m} \mathcal{K}^2 - \left\{ -\frac{\hbar^2}{2m} \frac{\partial^2}{\partial r^2} \mathbf{1} + \mathbf{U} + \mathbf{V} \right\} \right] \vec{\phi}_F = \vec{F} \quad (36)$$

where \vec{F} is the external field which is expressed as

$$\vec{F}(r) = \sum_{q=n,p} \vec{\varphi}_q f_q(r) \quad (37)$$

in the form of the $2(N_n + N_p)$ -dimensional vector. The solution of the RPA equation with the external field Eq.(36) $\vec{\phi}_F$ is given by using the Green function $\mathcal{G}^{(\pm)}(r, r')$ as

$$\vec{\phi}_F(r) = \int_0^\infty dr' \mathcal{G}^{(+)}(r, r') \cdot \vec{F}(r') \quad (38)$$

and the strength function is given by

$$\begin{aligned} S_F(\omega) &= -\frac{1}{\pi} \text{Im} \int dr \vec{F}^\top(r) \cdot \vec{\phi}_F(r) \\ &= -\frac{1}{\pi} \text{Im} \int \int dr dr' \vec{F}^\top(r) \cdot \mathcal{G}^{(+)}(r, r') \cdot \vec{F}(r') \end{aligned} \quad (39)$$

$$(40)$$

Since the inverse of the Wronskian is included in the Green function as shown in Eq.(35) and the Wronskian is related to the Jost function as shown by Eq.(30), the pole of the strength function may be found on the complex energy ω plane as a solution of

$$\det \mathcal{J}^{(+)}(\omega) = 0. \quad (41)$$

The strength function can also be expressed as

$$\begin{aligned} S_F(\omega) &= -\frac{1}{\pi} \int dr \sum_{q=n,p} f_q(r) \text{Im} \delta\rho_{F,q}(r) \\ &= -\frac{1}{\pi} \sum_{qq'} \int \int dr dr' f_q(r) \text{Im} R_{qq'}(r, r') f_{q'}(r') \end{aligned} \quad (42)$$

$$(43)$$

by using the density fluctuation $\delta\rho_{F,q}(r)$ and RPA response function $R_{qq'}(r, r')$ which were defined by

$$\delta\rho_{F,q}(r) = \vec{\varphi}_q^\top \cdot \vec{\phi}_F(r) \quad (44)$$

$$R_{qq'}(r, r') = \vec{\varphi}_q^\top \cdot \mathcal{G}^{(+)}(r, r') \cdot \vec{\varphi}_{q'} \quad (45)$$

Since $\vec{\phi}_F(r)$ is $2(N_n + N_p)$ -dimensional vector which is represented by

$$\vec{\phi}_F = \begin{pmatrix} \phi_{F,1}^{(n)} \\ \phi_{F,2}^{(n)} \\ \vdots \\ \phi_{F,N_n}^{(n)} \\ \phi_{F,1}^{(p)} \\ \phi_{F,2}^{(p)} \\ \vdots \\ \phi_{F,N_p}^{(p)} \end{pmatrix} \quad \text{with} \quad \phi_{F,\alpha}^{(q)} = \begin{pmatrix} X_{F,\alpha}^{(q)} \\ Y_{F,\alpha}^{(q)} \end{pmatrix}, \quad (46)$$

the density fluctuation $\delta\rho_{F,q}(r)$ can be decomposed by each transition component α as

$$\delta\rho_{F,q}(r) = \sum_{\alpha=1, N_q} \vec{\varphi}_\alpha^{(q)} \left(X_{F,\alpha}^{(q)}(r) + Y_{F,\alpha}^{(q)}(r) \right) \quad (47)$$

$$= \sum_{\alpha=1, N_q} \delta\rho_{F,q}^{(\alpha)}(r). \quad (48)$$

Note that the capability of such a transition component decomposition is one of the features of our RPA method using the Jost function. This is because the existing cRPA method cannot perform a transition component decomposition of density fluctuations because the density fluctuations or RPA response functions are directly obtained.

III. NUMERICAL SETUP AND CHECK

The first Riemann sheet on which the bound state exists is analytically connected to the Riemann sheet on which the pole of resonance exists by a branch cut line extending from the branching point given by the threshold energy on the real axis of complex energy. As will be discussed in more detail later in Sec.III C, there are as many Riemann sheets as there are sign combinations of the imaginary part of the complex momentum defining the complex energy plane, and the number of types of complex momentum is determined by the number of transition configurations (see Table II for $E1$ dipole of ^{16}O), so the heavier the nucleus, the more Riemann sheets that are defined. Therefore, in this paper the electric dipole excitations of ^{16}O (known as relatively light spherical nuclei) are calculated and analyzed using the Woods-Saxon potential for the mean field $U_{lj}^{(q)}(r)$ and simple density-dependent interactions for the residual interactions $\kappa_{qq'}$.

In this section, the model and parameters used in this paper and the results of a comparison with the cRPA method as a numerical check will be presented in Sec.III A and III B, respectively. In Sec.III C, an explanation of the definition of the

TABLE I. The bound single-particle levels for neutron and proton obtained by using the Woods-Saxon potential model. The unit is MeV.

	Neutron	Proton
$s_{1/2}$	-36.17	-31.16
$p_{3/2}$	-21.31	-16.84
$p_{1/2}$	-16.38	-11.95
$d_{5/2}$	-6.81	-2.95
$s_{1/2}$	-4.90	-1.43

Riemann sheet in ^{16}O electric dipole excitations and a numerical check of the analytic continuation is presented.

A. Model and parameters

The Woods-Saxon potential model and the parameters are given by

$$U_{lj}^{(n)}(r) = V_0^{(n)} f_{WS}(r) + V_1^{(n)} \mathbf{l} \cdot \mathbf{s} \frac{1}{r} \frac{df_{WS}(r)}{dr} + \frac{\hbar^2 l(l+1)}{2mr^2} \quad (49)$$

$$V_0^{(n)} = -60 \left(1 - 0.67 \frac{N-Z}{A} \right) \quad (50)$$

$$V_1^{(n)} = 15 \left(1 - 0.67 \frac{N-Z}{A} \right) \quad (51)$$

$$U_{lj}^{(p)}(r) = V_0^{(p)} f_{WS}(r) + V_1^{(p)} \mathbf{l} \cdot \mathbf{s} \frac{1}{r} \frac{df_{WS}(r)}{dr} + \frac{\hbar^2 l(l+1)}{2mr^2} + V_C(r) \quad (52)$$

$$V_0^{(p)} = -60 \left(1 + 0.67 \frac{N-Z}{A} \right) \quad (53)$$

$$V_1^{(p)} = 15 \left(1 + 0.67 \frac{N-Z}{A} \right) \quad (54)$$

$$f_{WS}(r) = \frac{1}{1 + \exp((r-R)/a)} \quad (55)$$

$$R = r_0(A-1)^{\frac{1}{3}} \quad (56)$$

$$r_0 = 1.2, \quad a = 0.65 \quad (57)$$

$$V_C(r) = \begin{cases} \frac{Ze^2}{2R} \left(3 - \left(\frac{r}{R} \right)^2 \right) & (r < R) \\ \frac{Ze^2}{r} & (r \geq R) \end{cases} \quad (58)$$

We adopt and use the following residual interaction model and parameters

$$\kappa_{qq} = \frac{1}{2} t_0 (1 - x_0) + \frac{t_3}{12} ((5 + x_3) \rho - (2 + 4x_3) \rho_q) \quad (59)$$

$$\begin{aligned} \kappa_{np} &= \kappa_{pn} \\ &= t_0 \left(1 + \frac{1}{2} x_0 \right) + \frac{t_3}{12} (5 + x_3) \rho \end{aligned} \quad (60)$$

with $t_0 = -1100 \text{ MeV fm}^3$, $t_3 = 16000 \text{ MeV fm}^6$, $x_0 = 0.5$ and $x_3 = 1.0$.

For the external field $f_q(r)$ in Eq.(37), we adopt

$$f_n(r) = e \frac{Z}{A} r \quad (61)$$

$$f_p(r) = -e \frac{N}{A} r \quad (62)$$

as an $E1$ dipole operator where $A = N + Z$, with $N = Z = 8$ for ^{16}O .

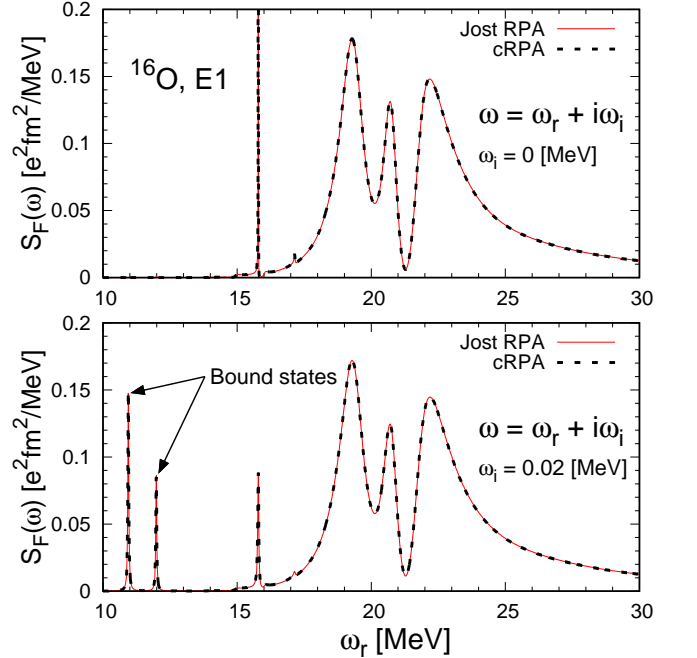


FIG. 1. (Color online) Comparison of the cRPA method (dotted curve) with the method we developed in this paper (Jost-RPA, solid curve) by the $E1$ dipole excitation strength of ^{16}O . The strength function S_F given as a function of complex energy ω is plotted as a function of the real part ω_r of complex energy. Note that in the upper and lower panels, the imaginary part of complex energy $\omega_i = 0$ and 0.02 MeV, respectively.

In this paper, we solved the simultaneous second-order differential equation Eq.(9) by taking into account the boundary condition of continuum in the coordinate space up to $r \leq 20$ fm with an equidistant interval $\Delta r = 0.2$ fm.

The single particle levels of neutron and proton for both hole and particle bound states which are obtained by using the

TABLE II. The combination of angular momenta for $L = 1$ associated with the configurations of the particle-hole excitations in the dipole excitations of ^{16}O and the subscript α that designates it for neutron and proton, respectively.

q (= n, p)	α	$[lj]_{\alpha}^{(q)}$	$[l_h j_h]_{\alpha}^{(q)}$	$e_{\alpha}^{(q)}$ [MeV]
(neutron part)				
n	1	$s_{1/2}$	$p_{1/2}$	-16.38
	2	$d_{3/2}$	$p_{1/2}$	-16.38
	3	$d_{5/2}$	$p_{3/2}$	-21.31
	4	$s_{1/2}$	$p_{3/2}$	-21.31
	5	$d_{3/2}$	$p_{3/2}$	-21.31
	6	$p_{3/2}$	$s_{1/2}$	-36.17
	7	$p_{1/2}$	$s_{1/2}$	-36.17
(proton part)				
p	1	$s_{1/2}$	$p_{1/2}$	-11.95
	2	$d_{3/2}$	$p_{1/2}$	-11.95
	3	$d_{5/2}$	$p_{3/2}$	-16.84
	4	$s_{1/2}$	$p_{3/2}$	-16.84
	5	$d_{3/2}$	$p_{3/2}$	-16.84
	6	$p_{3/2}$	$s_{1/2}$	-31.16
	7	$p_{1/2}$	$s_{1/2}$	-31.16

Woods-Saxon potential are shown in Table.I. The number assigned to the combination of angular momentum that couples with the angular momentum of the hole state to make $L=1$ is the subscription α shown in Table.II.

B. Comparison with cRPA method

The cRPA method and the Jost function method extended within the framework of the RPA theory developed in this paper (henceforth referred to as the Jost-RPA method) are the same method in the sense that the RPA calculation is performed by taking into account the boundary conditions of continuum. However, the cRPA and Jost-RPA methods are completely different in the sense that the equations to be solved are different.

The cRPA method calculates the unperturbed one-particle Green's function that satisfies the boundary conditions of the continuum and then calculates the unperturbed response function using it. The unperturbed response function is substituted into the Bethe-Salpeter equation, which is an integral equation equivalent to the RPA equation, and the RPA response function is obtained using the inverse matrix method in coordinate space. In contrast, the Jost-RPA method calculates the perturbed one-particle Green's function Eq.(35) using the regular and non-regular solutions obtained by directly solving the RPA equation given in the form of a differential equation Eq.(9), taking into account the boundary conditions of the continuum, and the Jost function (which is calculated using them). It is then used to calculate the RPA response function, Eq.(45).

Since the two methods are thus different, we compared the two methods in the $E1$ strength function. Both the cRPA and Jost-RPA methods allow the RPA response function to be calculated as a function of continuous complex energy. The strength function can be calculated using the RPA response function, as shown in Eq.(43). Fig.1 shows the $E1$ strength function for ^{16}O as a function of the real part of the complex energy (ω_r) using the cRPA and Jost-RPA methods. In the upper and lower panels, the imaginary part of the complex energy is set to $\omega_i = 0$ and 0.02 MeV, respectively. The comparison of the cRPA and Jost-RPA methods in the figure shows that the results of the cRPA and Jost-RPA methods are in perfect agreement.

Note that the peaks appearing in the energy region below threshold in the lower panel are bound states, but these are not seen in the upper panel. This is because the poles of the bound states appear on the real axis of the complex energy (i.e., they have no width) and cannot be plotted as a function of ω_r with $\omega_i = 0$. In contrast, the strength as background is due to the contribution of the continuum, and the resonance peaks when the width of the resonance (imaginary part of the pole) is very large compared to ω_i are less affected by ω_i and the shape of the strength function is almost unchanged. These are relatively well-known properties of cRPA, and one can clearly and easily distinguish between the bound states and the others.

Thus, the cRPA method can calculate the strength above the threshold, including the width, but it cannot quantitatively calculate the individual width of each resonance peak. In contrast, our Jost-RPA method can find the corresponding pole (real part is the resonance energy, imaginary part is the resonance width) for each resonance peak individually as the zeros of the Jost function on the complex energy Riemann sheet. The results are shown in the next section (Sec.IV).

C. Riemann sheets of the complex energy planes

The complex energy ω can be defined as a function of the complex momentum $k_{1,\alpha}^{(q)}$ and $k_{2,\alpha}^{(q)}$ (Eqs.(6) and (7)). According to the basics of complex analysis, the types of on the complex energy plane (Riemann sheets) are determined by the sign of the imaginary part of the complex momentum and its combinations. In the case of ^{16}O , three momentum can be defined for each of $k_{1,\alpha}^{(q)}$ and $k_{2,\alpha}^{(q)}$ for the proton and neutron, respectively, which means that 4,096 types of Riemann sheets can be defined mathematically. However, Riemann sheets in which the imaginary parts of $k_{1,\alpha}^{(q)}$ and $k_{2,\alpha}^{(q)}$ are simultaneously negative are unphysical. Therefore, there are a total of 128 types of physically meaningful Riemann sheets, 64 types each corresponding to the regions $\text{Re } \omega > 0$ and $\text{Re } \omega < 0$. Furthermore, there are only 12 types of Riemann sheets in total, 6 each in the regions $\text{Re } \omega > 0$ and $\text{Re } \omega < 0$, that are analytically connected on the real axis of ω with the first Riemann sheet (ω_0), where the imaginary part of all momentum is defined as positive. The definitions of ω_0 and the 12 types of

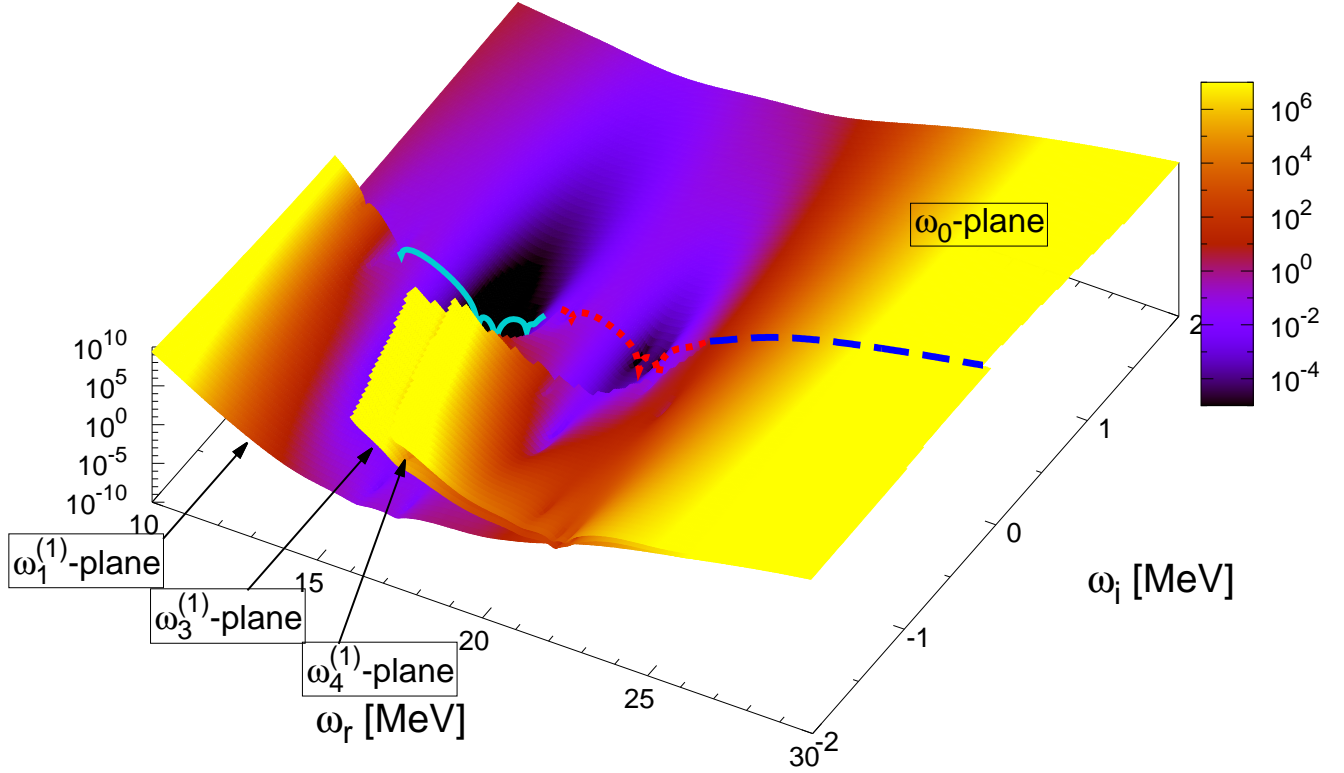


FIG. 2. (Color online) $|\det \mathcal{J}|$ plotted as a function of the complex energy ω . The values of $|\det \mathcal{J}|$ with the complex energy defined as the first Riemann sheet (ω_0) is shown in the $\text{Im } \omega_i > 0$ region. $|\det \mathcal{J}|$ with $\omega_1^{(1)}$, $\omega_3^{(1)}$ and $\omega_4^{(1)}$ are shown in the $\text{Im } \omega_i < 0$ region. And they are connected at the branch-cut lines which are existing on the real axis continuously. The sky-blue solid, red dotted and blue dashed curves are the branch cut lines which connect ω_0 with $\omega_1^{(1)}$, $\omega_3^{(1)}$ and $\omega_4^{(1)}$, respectively.

Riemann sheets are shown below.

$$\omega_0 = \omega(\text{Im } k_{1,\alpha}^{(q)} > 0, \text{Im } k_{2,\alpha}^{(q)} > 0) \quad \text{for all } \alpha \text{ and } q \quad (63)$$

$$\omega_4^{(s)} = \omega(\text{Im } k_{s,\alpha}^{(q)} < 0 \text{ for } e_\alpha^{(q)} \geq -21.31) \quad \text{other } \text{Im } k_{1,\alpha}^{(q)} \text{ and } \text{Im } k_{2,\alpha}^{(q)} \text{ are positive,} \quad (67)$$

$$\omega_1^{(s)} = \omega(\text{Im } k_{s,\alpha}^{(q)} < 0 \text{ for } e_\alpha^{(q)} = -11.95) \quad \text{other } \text{Im } k_{1,\alpha}^{(q)} \text{ and } \text{Im } k_{2,\alpha}^{(q)} \text{ are positive,} \quad (64)$$

$$\omega_5^{(s)} = \omega(\text{Im } k_{s,\alpha}^{(q)} < 0 \text{ for } e_\alpha^{(q)} \geq -31.16) \quad \text{other } \text{Im } k_{1,\alpha}^{(q)} \text{ and } \text{Im } k_{2,\alpha}^{(q)} \text{ are positive,} \quad (68)$$

$$\omega_2^{(s)} = \omega(\text{Im } k_{s,\alpha}^{(q)} < 0 \text{ for } e_\alpha^{(q)} \geq -16.38) \quad \text{other } \text{Im } k_{1,\alpha}^{(q)} \text{ and } \text{Im } k_{2,\alpha}^{(q)} \text{ are positive,} \quad (65)$$

$$\omega_6^{(s)} = \omega(\text{Im } k_{s,\alpha}^{(q)} < 0 \text{ for } e_\alpha^{(q)} \geq -36.17) \quad \text{other } \text{Im } k_{1,\alpha}^{(q)} \text{ and } \text{Im } k_{2,\alpha}^{(q)} \text{ are positive,} \quad (69)$$

$$\omega_3^{(s)} = \omega(\text{Im } k_{s,\alpha}^{(q)} < 0 \text{ for } e_\alpha^{(q)} \geq -16.84) \quad \text{other } \text{Im } k_{1,\alpha}^{(q)} \text{ and } \text{Im } k_{2,\alpha}^{(q)} \text{ are positive,} \quad (66)$$

where $s = 1, 2$. Riemann sheets $\omega_{1-6}^{(1)}$ are expected to be connected with ω_0 at $11.95 \leq \text{Re } \omega \leq 16.38$ MeV, $16.38 \leq \text{Re } \omega \leq 16.84$ MeV, $16.84 \leq \text{Re } \omega \leq 21.31$ MeV, $21.31 \leq \text{Re } \omega \leq 31.16$ MeV, and $31.16 \leq \text{Re } \omega \leq 36.17$

MeV, respectively. And $\omega_{1-6}^{(2)}$ are expected to be connected with ω_0 in the negative energy region. We confirmed these analytical continuation numerically in Fig.2.

In Fig.2 we show $|\det \mathcal{J}|$ calculated using ω_0 in the region $\omega_i > 0$, and in the region $\omega_i < 0$ we show $|\det \mathcal{J}|$ calculated using the Riemann sheets ($\omega_1^{(1)}$, $\omega_3^{(1)}$ and $\omega_4^{(1)}$ -planes) connected to ω_0 in the region $\omega_r < 30$ MeV ($\omega_2^{(1)}$ is also connected with ω_0 in a very narrow region $16.38 < \omega_r < 16.84$ MeV but is not shown in this figure for ease of seeing the figure).

IV. ANALYSIS

A. Poles of $E1$ strength of ^{16}O on the complex energy plane

The solution of Eq.(9) is given at the zero point of the Jost function (i.e. the value of complex energy ω that satisfies Eq.(41)) and the bound states appear on the real axis of complex energy below the threshold. It is believed that the poles of the resonance state exists on the Riemann sheet that is analytically connected to the first Riemann sheet (ω_0 -plane) on the real axis above threshold. The real part of the resonance pole gives the resonance energy, and the imaginary part the half-width of the resonance. However, the poles exhibited by $|\det \mathcal{J}| = 0$ also include unphysical ones due to hole-hole excited configurations, which are known to cancel at the level of the unperturbed response function and do not contribute to the strength function, and they appear on the real axis of the complex energy. In Fig.2, such unphysical poles appear at $\omega_r = 19.21$ MeV and 19.79 MeV. The presence of such unphysical poles makes it difficult to see the physical poles that exist near the real axis when $|\det \mathcal{J}|$ is plotted on the complex energy plane. Considering the property that the poles of resonances which have widths existing above the threshold do not appear on the real axis, $\frac{|\det \mathcal{J}(\omega_i^{(1)})|}{|\det \mathcal{J}(\omega_0)|}$ (for $i \in 1, 3, 4$) is plotted instead of $|\det \mathcal{J}|$ in Fig.3 in order to find the poles corresponding to the resonances.

The top panel of Fig. 3 shows the $E1$ strength function of ^{16}O as a function of ω_r with $\omega_i = 0$ MeV, in order to see the correspondence between the poles on the complex energy plane and the peaks of the strength function. Fig.4 is an enlarged view of the region of $-0.01 \leq \omega_i \leq 0.0$ MeV and $15.77 \leq \omega_r \leq 15.81$ MeV of $\omega_1^{(1)}$ -plane near the low-lying peak in Fig.3. The pole that can be moved to the first Riemann sheet by rotating the branch cut line that analytically connects the first Riemann sheet (ω_0 -plane) to the other Riemann sheets on the complex energy around the branch point, e.g. by complex scaling, is the pole of resonance, which contributes as a peak to the strength function. The poles shown as (a)-(g) in Fig.3 are the poles that are considered to contribute to the peak of the strength function. Their values of (a)-(g) are given in the second column of Table.III.

Each of these poles found in the complex plane is considered to be linearly independent, and the giant electric $E1$ dipole resonance seems to be formed by four independent

poles (d), (e), (f), and (g) from Fig.3. This result shows that, at least within the framework of RPA theory, one of the features of giant resonances, the 'large width', is not given by the imaginary part of a single pole, but is formed by several independent poles. In the following subsections, further analysis will be carried out to investigate the properties of each of the poles.

B. Trajectories of poles as a response to residual interactions

Multiplying the residual interactions κ_{qq} (for both κ_{nn} and κ_{pp}) and κ_{np} by constants f_1 and f_2 , respectively, as $\kappa_{qq} \rightarrow f_1 \times \kappa_{qq}$, $\kappa_{np} \rightarrow f_2 \times \kappa_{np}$, and varying them from 0 to 1, the trajectories of the poles can be drawn as shown in the bottom panel of Fig.5. The top three panels show, in order from top to bottom, the RPA strength function ($f_1 = f_2 = 1$), the RPA strength function with $f_1 = 1$ and $f_2 = 0$ (i.e. $\kappa_{np} = 0$) and the unperturbed strength function ($f_1 = f_2 = 0$, i.e. $\kappa_{qq} = 0$). The positions of the poles corresponding to the peaks of the RPA strength function, the RPA strength function with $\kappa_{np} = 0$ and the unperturbed strength function are shown by circle (\bullet), square (\square) and triangle (\triangle) symbols respectively in the bottom panel. The specific values of the circle (\bullet), square (\square) and triangle (\triangle) for the poles in (a)-(g) are given in columns 2, 3 and 4 of Table III, respectively.

Focus on poles (d), (e), (f) and (g), which seem to be related to giant resonances. It can be seen from Fig.5 that, first of all, poles (d), (e), (f) and (g) have different origins. The pole (d) arises from the pole of the unperturbed neutron resonance of $\nu \left[d_{3/2} \otimes (p_{1/2})^{-1} \right]_1$ at $16.58 - i1.33 \times 10^{-3}$ MeV. This unperturbed neutron resonance appears as a very sharp peak in the unperturbed strength function. The pole (e) is almost unaffected by residual interactions and no corresponding peak in the unperturbed strength function. This is thought to be a shape resonance created by a mean field with a very wide width and only a small contribution as background of the strength function. The pole (f) originates from the unperturbed proton resonance of $\pi \left[d_{3/2} \otimes (p_{3/2})^{-1} \right]_1$ at $20.36 - i0.26$ MeV and appears in the unperturbed strength function as a peak with a rather broad width. The effect of residual interactions is small. The pole (g) arises from the pole of the unperturbed neutron resonance of $\nu \left[d_{3/2} \otimes (p_{3/2})^{-1} \right]_1$ at $21.50 - i1.3 \times 10^{-3}$ MeV. This unperturbed neutron resonance appears as a very sharp peak in the unperturbed strength function.

The influence of the residual interactions is remarkable for poles (d) and (g), both of which originate from the poles of the neutron unperturbed resonance. As κ_{np} increases, both the resonance energy (real part of the pole) and the width (imaginary part of the pole) of the pole (d) increase significantly. The significant shift of the resonance energy of the $E1$ dipole resonance to higher energy due to residual interactions is a typical property of the collective excited state shown by the schematic model [8]. However, the response property of the pole (d) to the residual interaction is not only the resonance

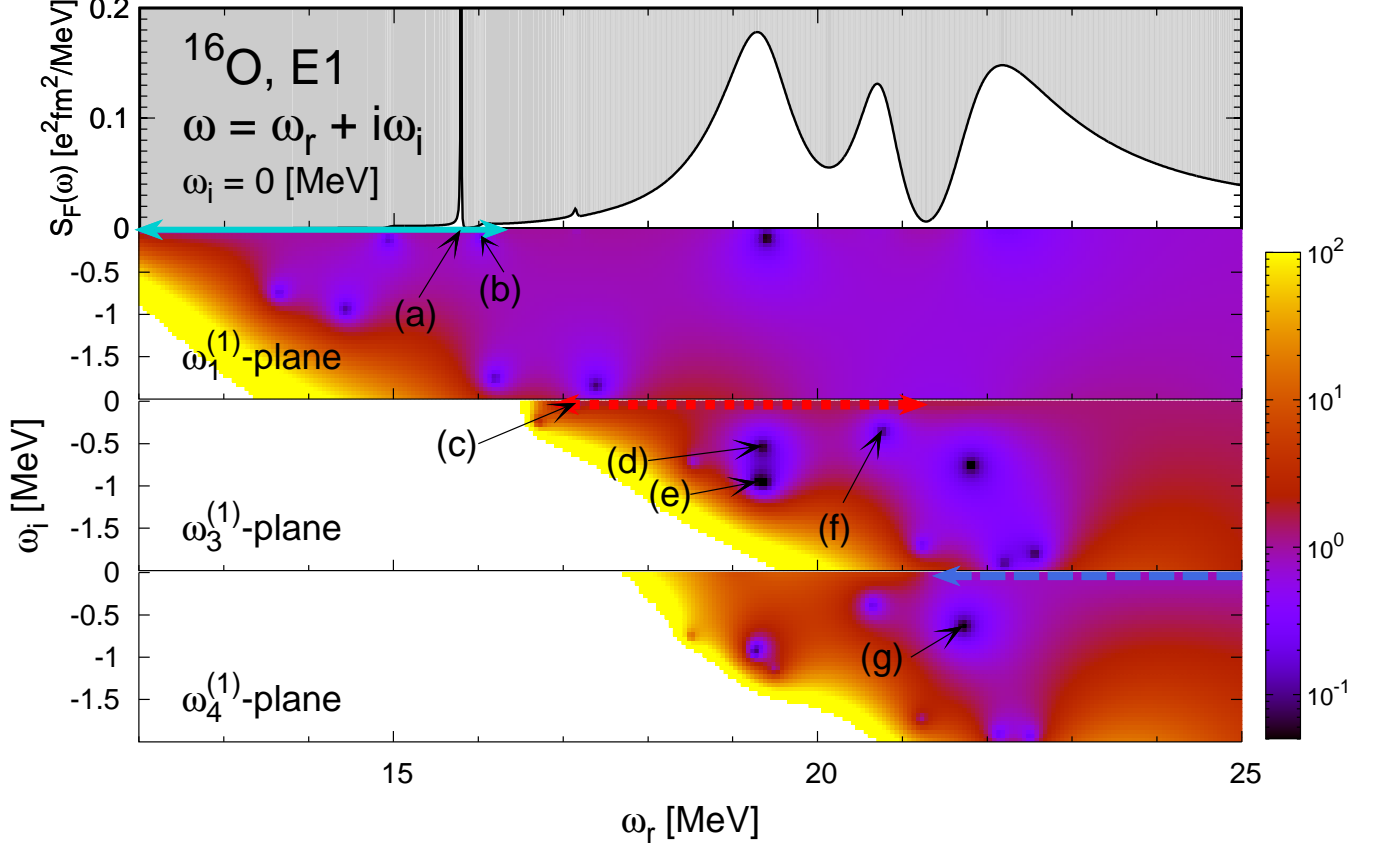


FIG. 3. (Color online) The $E1$ strength function of ^{16}O plotted as a function of ω_r with $\omega_i = 0$ MeV in the upper panel, and $|\det \mathcal{J}(\omega_i^{(1)})|/|\det \mathcal{J}(\omega_0)|$ for $i \in 1, 3$ and 4 in the lower three panels. The poles labeled (a)-(g) are poles which can contribute to the strength function. The sky-blue solid, red dotted and blue dashed lines (with both side arrows) denote the branch cut lines for three Riemann sheets ($\omega_1^{(1)}$, $\omega_3^{(1)}$ and $\omega_4^{(1)}$) which connect with the first Riemann sheet (ω_0).

TABLE III. The values of poles ((a)-(g)) on the complex energy planes, which are calculated by the RPA, RPA with $\kappa_{np} = 0$ and the unperturbed response, which are corresponding to the filled circle (\bullet), square (\square) and triangle (\triangle) symbols shown in the lower panel of Fig.5.

Pole	RPA [MeV]	RPA with $\kappa_{np} = 0$ [MeV]	Unperturbed($\kappa_{qq'} = 0$) [MeV]	Riemann surface
(a)	$15.79 - i3.35 \times 10^{-3}$	$15.48 - i0.15$	$15.47 - i0.26$	$\omega_1^{(1)}$ -plane
(b)	$16.03 - i0.07$	$16.16 - i0.18$	$15.47 - i0.26$	
(c)	$17.15 - i0.02$	$16.59 - i1.39 \times 10^{-3}$	$16.58 - i1.33 \times 10^{-3}$	$\omega_3^{(1)}$ -plane
(d)	$19.34 - i0.53$	$17.32 - i3.64 \times 10^{-2}$	$16.58 - i1.33 \times 10^{-3}$	
(e)	$19.28 - i0.95$	$19.32 - i0.92$	$19.32 - i0.92$	
(f)	$20.76 - i0.34$	$20.41 - i0.27$	$20.36 - i0.26$	
(g)	$21.71 - i0.63$	$21.58 - i7.45 \times 10^{-3}$	$21.50 - i1.33 \times 10^{-3}$	$\omega_4^{(1)}$ -plane

energy (the real part of the pole) shift to higher energy, but also the significant increase in the width (the imaginary part of the pole). In the case of the pole (g), the response to the residual interaction shows almost no energy shift, but a remarkable increase in the width. This implies that this is mainly due to the dominance of coupling with the non-resonant continuum. And this may be related to the fact that only the pole (g) lies on a different Riemann sheet from the other resonances, and

there is no proton-originated pole on the same Riemann sheet (see Fig.3).

Poles (d) and (f) originate from the poles of the neutron and proton unperturbed resonances, respectively, so they originally belong to different Riemann sheets. However, the κ_{np} effect mixes the neutron and proton components so that (d) and (f) are finally poles belonging to the same Riemann sheet. However, pole (f) has a very small energy shift, and its width

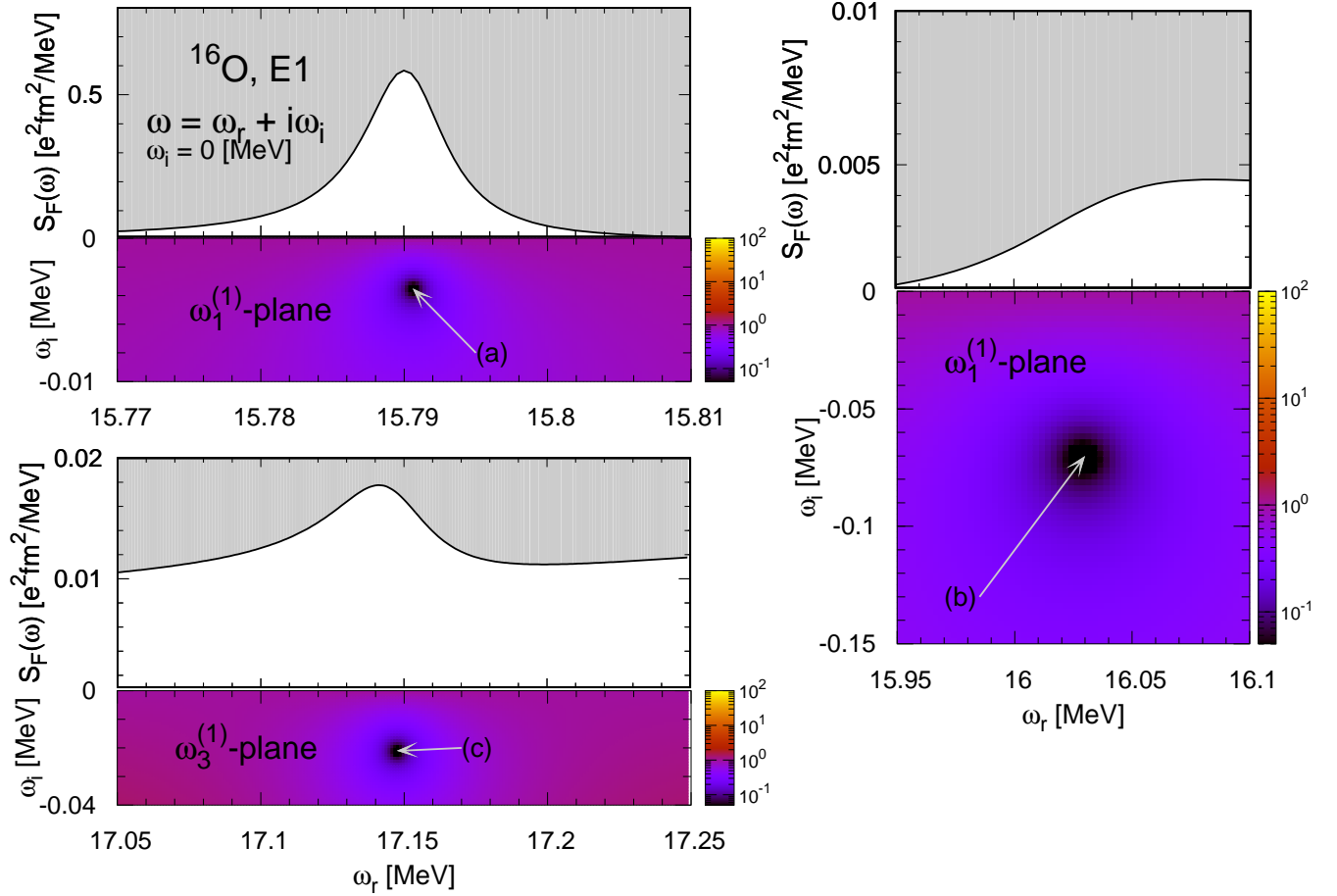


FIG. 4. (Color online) In Fig. 3, the poles (a), (b), and (c), which are located very close to the real axis of the complex energy plane, are shown enlarged.

does not change much compared to pole (d). This may be due to the fact that the unperturbed resonance (shape resonance) character tends to remain stronger at pole (f) due to the Coulomb barrier.

C. Component structure analysis of density fluctuations

In the Jost-RPA method, the density fluctuation $\delta\rho_{F,q}(r)$ is defined by Eq.(44) and can be decomposed into components with subscription α , as shown in Eq.(48). Fig. 6 and 7 show the imaginary part of the RPA density fluctuations and unperturbed density fluctuations for poles (d), (f) and (g), respectively. The energy of the density fluctuations is the real part of the poles, *i.e.*, on the real axis of the complex energy plane ($\omega_i = 0$). In each figure, the density fluctuations for protons and neutrons are shown in the upper panel by solid curves, while the density fluctuations for the $\alpha = 2, 3$ and 6 components added together are shown by dotted curves. In the middle and lower panels, the main contributing components are shown when the proton and neutron density fluctuations are decomposed into transition components, respectively. Note

that the density fluctuations shown in these figures are normalized by the value of the strength function S_F at a given energy (ω_r).

Looking at the solid curves in the top panels of Fig. 6, the density fluctuations at poles (d) and (f) both roughly show the neutron density and proton density oscillating in antiphase, which is a typical feature of the collective motion of isovector dipole excitations. The density fluctuations of the pole (g) also show movement of the neutron and proton densities in antiphase, but the proton density is likely to jump out of the nucleus.

In the case of the pole (d) (originating from the neutron unperturbed transition $\alpha = 2$, *i.e.* $\nu [d_{3/2} \otimes (p_{1/2})^{-1}]_1$), both proton and neutron components ($\delta\rho_{F,p}$ and $\delta\rho_{F,n}$) consist of a superposition of in-phase $\alpha = 2, 3$ and 6 components, plus $\alpha = 4$ and 5 components with antiphase. In the case of the pole (f) (originating from the proton unperturbed transition $\alpha = 5$, *i.e.* $\pi [d_{3/2} \otimes (p_{3/2})^{-1}]_1$), the $\alpha = 5$ component in the proton component $\delta\rho_{F,p}$ is enhanced by the in-phase superposition of the $\alpha = 2, 3$ and 6 components, to which the antiphase $\alpha = 4$ component is added.

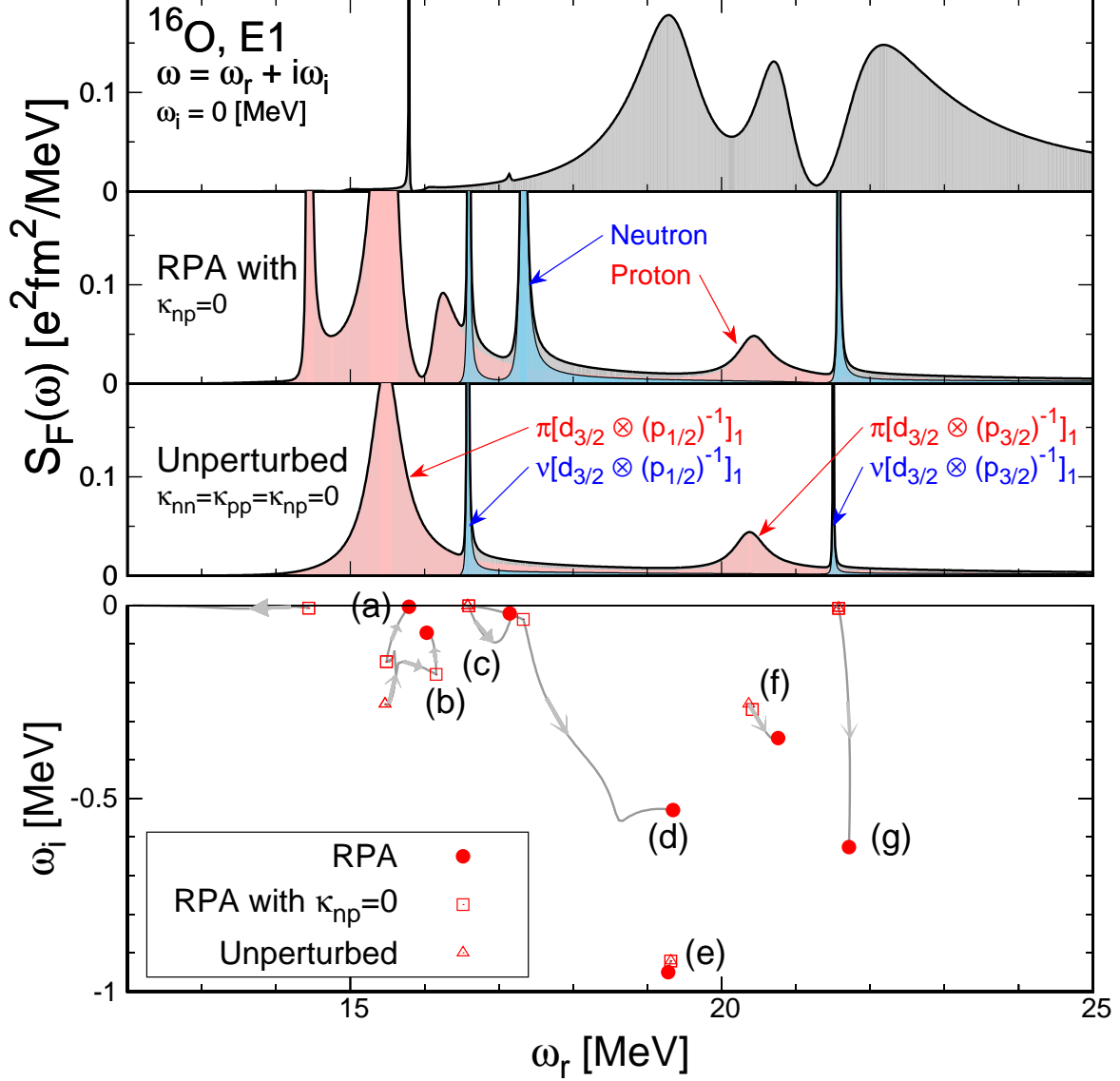


FIG. 5. (Color online) The $E1$ strength function which is calculated by RPA, RPA with $\kappa_{np} = 0$, and the unperturbed response shown in the upper three panels. Trajectories of poles (a)-(g) which shows the connection between the RPA and unperturbed response, obtained by varying the constant parameters f_1 and f_2 multiplied to the residual interaction are shown in the lower panel. The filled circle (\bullet), square (\square) and triangle (\triangle) symbols show the position of poles which are calculated by the RPA (*i.e.* $f_1 = 1, f_2 = 1$), RPA with $\kappa_{np} = 0$ ($f_1 = 1, f_2 = 0$) and unperturbed ($f_1 = 0, f_2 = 0$) solutions, respectively. (See text and Table III)

The neutron components $\delta\rho_{F,n}$ consists of a superposition of in-phase $\alpha = 2, 3$ and 6 components, plus $\alpha = 4$ and 5 components with antiphase. In the case of the pole (g) (originating from the neutron unperturbed transition $\alpha = 5$, *i.e.* $\nu[d_{3/2} \otimes (p_{3/2})^{-1}]_1$), the proton component $\delta\rho_{F,p}$ is in the form that the intranuclear part ($r < 3$ fm region) of the amplitude created by the in-phase superposition of the $\alpha = 2, 3$ and 6 components is damped by the $\alpha = 4$ component, leaving mainly only the extranuclear component. The neutron component $\delta\rho_{F,n}$ is dominated by the $\alpha = 5$ component and the

influence of the other components is relatively small.

The component structure of the density fluctuations of pole (d) is roughly antiphase to each other for neutrons and protons, whereas the density fluctuations of pole (f) have a neutron component very similar to that of pole (d), but the proton component does not have the antiphase structure of neutrons. This may be because the proton component still keeps its unperturbed resonance (shape resonance) character due to the Coulomb barrier, although poles (d) and (f) influence each other by belonging to the same Riemann sheet. Or it could be that pole (d) and pole (f) overlap each other due to their wide

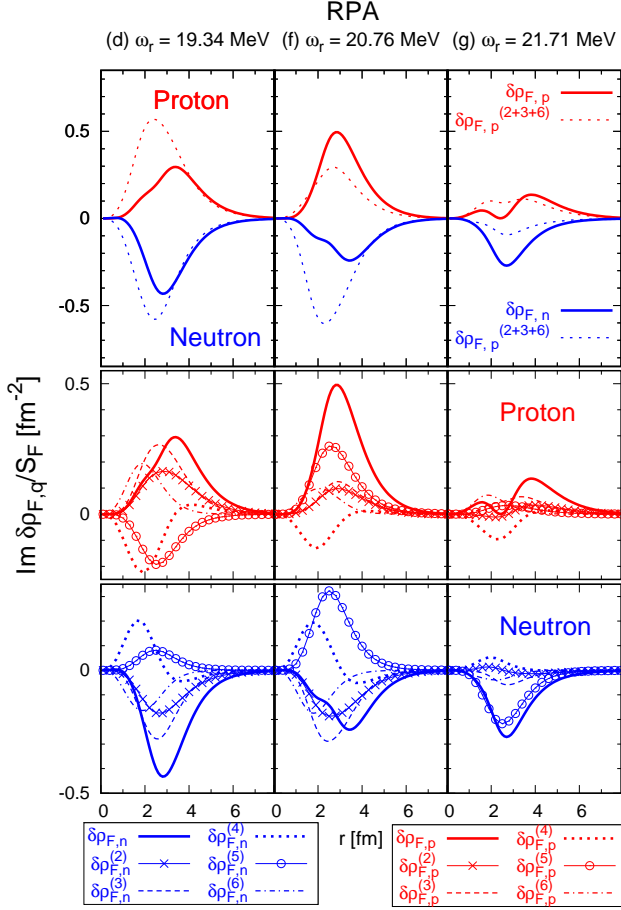


FIG. 6. (Color online) The density fluctuations $\delta\rho_F$ defined by Eq.(44) for the poles (d), (f) and (g) which are expected to be related with the giant dipole resonance are shown in the top panels by the red solid (for proton) and blue solid (for neutron) curves. The dotted curves show the summation of the $\alpha = 2, 3$ and 6 components. Component decomposition of the density fluctuation for proton and neutron are shown in the middle and bottom panels, respectively.

widths, and the component structure of pole (d) just appears in the component structure of the density fluctuations of pole (f), but actually pole (f) itself is a shape resonance with little effect from residual interactions.

The component structure of the density fluctuations of the pole (g) is very different from that of the poles (d) and (f). This may be due to the fact that pole (g) belongs to a different Riemann sheet than (d) and (f). The difference in component structure between protons and neutrons is assumed to be due to the fact that only unperturbed resonances (shape resonances) of neutrons exist in the same Riemann sheet. This may mean that, when the $E1$ excitation occurs, in which the neutron and proton move in opposite phases, the neutron tends to stay in the nucleus due to the characteristic of shape resonance, while the proton mainly couples to the nonresonant continuum and tends to move away from the nucleus.

These are inferences based on the analysis which we have done in this paper. In order to clarify whether the inferences

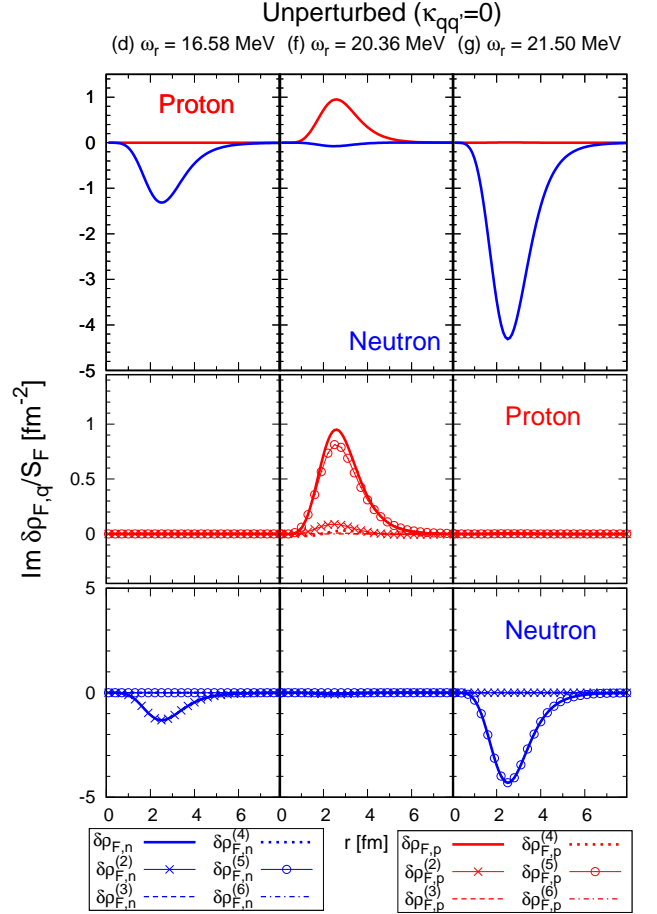


FIG. 7. (Color online) The same figure with Fig.6 but calculated with the unperturbed response ($\kappa_{qq'} = 0$).

are correct, it is necessary to analyze the pole-by-pole contribution to the strength function and density fluctuations, excluding overlaps from other resonances, etc. However, this requires changing the completeness of the system using the complex scaling method [16] or Berggren's method [17], because the completeness of the system is defined by the first Riemann sheet [18] (The contribution of resonances is not explicitly included in the completeness). These issues are for the future.

For the moment, the analysis at the current stage of this paper has shown that poles (d), (f) and (g), which may be related to the $E1$ giant dipole resonance, basically differ in their properties (resonance energy, width, response to residual interactions, component structure of density fluctuations) for each pole. Especially when a pole belongs to a different Riemann sheet from the others (e.g. pole (g)), the properties are more markedly different.

V. SUMMARY AND PERSPECTIVE

In this paper, the Jost function method is extended within the framework of RPA theory to find the complex eigenvalues

of the RPA equation on the complex energy plane (Jost-RPA method). As a first application of the Jost-RPA method, we chose ^{16}O electric dipole excitations and performed numerical calculations using the Woods-Saxon potential as the mean field and simple density-dependent interactions as the residual interactions. The cRPA and Jost-RPA methods are identical in terms of solving the RPA problem by considering the boundary conditions of the continuum, but the methods for solving the equations are completely different. Therefore, we first compared both methods by calculating the $E1$ strength function using the same potentials and residual interactions. It was found that the result of the Jost-RPA method is in perfect agreement with the result of the cRPA method.

In the original Jost function method, it is known that the complex energy eigenvalues of the system are obtained as the zeros of the Jost function on the complex energy plane that is analytically connected to the first Riemann sheet on the branch cut line. In the Jost-RPA method, a very large number of complex-energy Riemann sheets are defined, even for ^{16}O $E1$ excitations. However, only a very limited number of Riemann sheets are analytically connected to the first Riemann sheet by a branch cut line with a branch point at the threshold of each configuration on the real axis of complex energy. We checked numerically whether the Jost functions computed on those Riemann sheets actually have an analytical connection with the first Riemann sheet. Then, the poles (complex energy eigenvalues) corresponding to the peaks of the $E1$ strength function were successfully found numerically on the complex energy plane in analytical connection with the first Riemann sheet.

The poles found on the complex energy plane revealed that the $E1$ giant dipole resonance of ^{16}O is formed by three independent poles with different resonance energies and widths. Two of these three poles belong to the same Riemann sheet, and only one belongs to a different Riemann sheet. Trajectory analysis of the poles in terms of their response to residual interactions also shows that these three poles originate from different poles of unperturbed resonance and that the character of their response to residual interactions is also different for each pole. It was found that response characteristics to the residual interaction differed from pole to pole: a pole shifted towards higher energies with increasing width as the residual interaction became stronger, another pole was less affected by the residual interaction, and another pole only increased in width. The component structure of the density fluctuations is also characteristic for each pole, but the interpretation is not clear because of the possibility of overlap due to the width of the poles (especially for poles belonging to the same Riemann sheet). Only one thing is clear: the poles belonging to different Riemann sheets seem to have little influence on each other and to have quite different properties.

Based on the residue theorem in complex function theory, it is possible to extract and show the contribution of a specific pole in the complex plane in terms of physical quantities such as density fluctuations or strength functions. However, the completeness of the system is defined by the first Riemann sheet, and the resonance poles are not explicitly included in the completeness. Therefore, in order to apply the residue

theorem for more detailed analysis, the completeness must be modified using the complex scaling method or Berggren's method. Further analysis by improving the Jost-RPA method in this direction is expected to clarify points that were unclear in the analysis of this paper.

In this paper, RPA calculations for $E1$ dipole excitations of ^{16}O have been performed using the Woods-Saxon potential for the mean field and simple density-dependent interactions for the residual interactions, but other excitation modes and other nuclei are naturally of interest. However, for a more quantitatively reliable analysis, it is also important to perform self-consistent calculations [19–21] based on effective two-body nuclear forces, such as the Skyrme interactions [22–28]. This is because it is well known that calculations that break the self-consistency do not satisfy the sum rule for dipole excitations [29], and there is no phenomenological potential model for cases such as neutron-rich nuclei. Removing spurious modes is another important issue [8, 30–32]. In this paper, an approximation to remove the spurious mode from the external field was used, but this approximation may not work well in some cases, so it is preferable to remove it directly from the RPA solution. The cRPA has already developed a method to remove the spurious mode from the RPA response function [33]. A method to remove the spurious mode directly from the solution should also be developed for the Jost-RPA method.

We are planning to continue our research using the Jost-RPA method developed in this paper, improving the above-mentioned issues step by step, in order to further analyze and understand the excited structure of nuclei in more detail from the viewpoint of the resonance poles in the near future.

ACKNOWLEDGMENTS

This work is funded by Vietnam National Foundation for Science and Technology Development (NAFOSTED) under grant number “103.04-2019.329”. Tran Dieu Thuy was funded by the Master, PhD Scholarship Programme of Vingroup Innovation Foundation (VINIF), code VINIF.2022.TS128. This work was partially supported by the Hue University under the Core Research Program, grant No. NCM.DHH.2018.09.

1. Proof of Eq.(35)

The Green's theorem can lead the following equations

$$\begin{aligned} & \left[\Phi_0^{(r)\top}(r) \frac{\partial}{\partial r} \Phi^{(r)}(r) - \left(\frac{\partial}{\partial r} \Phi_0^{(r)\top}(r) \right) \Phi^{(r)}(r) \right] \\ &= \frac{2m}{\hbar^2} \int_0^r dr' \Phi_0^{(r)\top}(r') \mathcal{V}(r') \Phi^{(r)}(r') \end{aligned} \quad (70)$$

$$\begin{aligned}
& \pm i \mathcal{K}^{-1} \mathcal{J}_0^{(\pm)} \\
& - \left[\Phi_0^{(r)\top}(r) \frac{\partial}{\partial r} \Phi^{(\pm)}(r) - \left(\frac{\partial}{\partial r} \Phi_0^{(r)\top}(r) \right) \Phi^{(\pm)}(r) \right] \\
& = \frac{2m}{\hbar^2} \int_r^\infty dr' \Phi_0^{(r)\top}(r') \mathcal{V}(r') \Phi^{(\pm)}(r') \quad (71)
\end{aligned}$$

where $\Phi_0^{(r)}(r)$ and $\Phi_0^{(\pm)}(r)$ are regular and irregular solution matrix of

$$\left[\frac{\hbar^2}{2m} \mathcal{K}^2 - \left\{ -\frac{\hbar^2}{2m} \frac{\partial^2}{\partial r^2} \mathbf{1} + \mathcal{U} \right\} \right] \Phi_0^{(r)} = \mathbf{0} \quad (72)$$

and

$$\left[\frac{\hbar^2}{2m} \mathcal{K}^2 - \left\{ -\frac{\hbar^2}{2m} \frac{\partial^2}{\partial r^2} \mathbf{1} + \mathcal{U} \right\} \right] \Phi_0^{(\pm)} = \mathbf{0}, \quad (73)$$

respectively. And $\mathcal{J}_0^{(\pm)}$ is the Jost function which is defined by $\Phi_0^{(r)}(r)$ and $\Phi_0^{(\pm)}(r)$. It should be noted that $\Phi_0^{(r)}(r)$, $\Phi_0^{(\pm)}(r)$ and $\mathcal{J}_0^{(\pm)}$ are given as the $2(N_n + N_p) \times 2(N_n + N_p)$ diagonal matrix due to the absence of the residual interaction \mathcal{V} which has the off-diagonal components.

Introducing a $2(N_n + N_p) \times 2(N_n + N_p)$ dimensional matrix \mathcal{C} and calculating $\Phi^{(\pm)}(r) \mathcal{C} \times (\text{Eq.(70)})^\top + \Phi^{(r)}(r) \mathcal{C}^\top \times (\text{Eq.(71)})^\top$, we can obtain

$$\begin{aligned}
& \pm i \Phi^{(r)}(r) \mathcal{C}^\top \mathcal{J}_0^{(\pm)} \mathcal{K}^{-1} \\
& + \left[\Phi^{(\pm)}(r) \mathcal{C} \left(\frac{\partial}{\partial r} \Phi^{(r)\top}(r) \right) \right. \\
& \quad \left. - \Phi^{(r)}(r) \mathcal{C}^\top \left(\frac{\partial}{\partial r} \Phi^{(\pm)\top}(r) \right) \right] \Phi_0^{(r)}(r) \\
& - \left[\Phi^{(\pm)}(r) \mathcal{C} \Phi^{(r)\top}(r) \right. \\
& \quad \left. - \Phi^{(r)}(r) \mathcal{C}^\top \Phi^{(\pm)\top}(r) \right] \left(\frac{\partial}{\partial r} \Phi_0^{(r)}(r) \right) \\
& = \frac{2m}{\hbar^2} \Phi^{(r)}(r) \mathcal{C}^\top \int_r^\infty dr' \Phi^{(\pm)\top}(r') \mathcal{V}(r') \Phi_0^{(r)}(r') \\
& + \frac{2m}{\hbar^2} \Phi^{(\pm)}(r) \mathcal{C} \int_0^r dr' \Phi^{(r)\top}(r') \mathcal{V}(r') \Phi_0^{(r)}(r') \quad (74)
\end{aligned}$$

If we require

$$\left[\Phi^{(\pm)}(r) \mathcal{C} \left(\frac{\partial}{\partial r} \Phi^{(r)\top}(r) \right) \right. \\
\left. - \Phi^{(r)}(r) \mathcal{C}^\top \left(\frac{\partial}{\partial r} \Phi^{(\pm)\top}(r) \right) \right] = -\mathbf{1} \quad (75)$$

$$\left[\Phi^{(\pm)}(r) \mathcal{C} \Phi^{(r)\top}(r) \right. \\
\left. - \Phi^{(r)}(r) \mathcal{C}^\top \Phi^{(\pm)\top}(r) \right] = \mathbf{0}, \quad (76)$$

then we can rewrite Eq.(74) as

$$\begin{aligned}
& \pm i \Phi^{(r)}(r) \mathcal{C}^\top \mathcal{J}_0^{(\pm)} \mathcal{K}^{-1} - \Phi_0^{(r)}(r) \\
& = \frac{2m}{\hbar^2} \Phi^{(r)}(r) \mathcal{C}^\top \int_r^\infty dr' \Phi^{(\pm)\top}(r') \mathcal{V}(r') \Phi_0^{(r)}(r') \\
& + \frac{2m}{\hbar^2} \Phi^{(\pm)}(r) \mathcal{C} \int_0^r dr' \Phi^{(r)\top}(r') \mathcal{V}(r') \Phi_0^{(r)}(r'). \quad (77)
\end{aligned}$$

By taking the “trace” of Eqs.(75) and (76), and applying the following basic properties of the trace of the matrix

$$(i) \text{Tr}[AB] = \text{Tr}[BA]$$

$$(ii) \text{Tr}[A + B] = \text{Tr}[A] + \text{Tr}[B]$$

$$(iii) \text{Tr}[A^\top B] = \text{Tr}[AB^\top] = \text{Tr}[B^\top A] = \text{Tr}[BA^\top],$$

we can notice that Eq.(75) becomes

$$\frac{2m}{\hbar^2} \text{Tr}[\mathcal{C} \mathcal{W}^{(\pm)}] = \text{Tr}[\mathbf{1}], \quad (78)$$

and Eq.(76) is a trivial identity. Therefore we find

$$\mathcal{C} = \frac{\hbar^2}{2m} \mathcal{W}^{(\pm)-1} = \pm \frac{1}{i} \mathcal{K} \mathcal{J}^{(\pm)-1}. \quad (79)$$

By inserting Eq.(79) into Eq.(77), finally we can derive

$$\begin{aligned}
& \Psi^{(\pm)}(r) \\
& = \Psi_0^{(\pm)}(r) + \int_0^\infty dr' \mathcal{G}^{(\pm)}(r, r') \mathcal{V}(r') \Psi_0^{(\pm)}(r') \quad (80)
\end{aligned}$$

with use of the definition of the Green’s function Eq.(35), where $\Psi^{(\pm)}(r)$ and $\Psi_0^{(\pm)}(r)$ are the RPA and unperturbed “scattering” wave functions defined by

$$\Psi^{(\pm)}(r) = \Phi^{(r)}(r) \mathcal{J}^{(\pm)-1} \quad (81)$$

$$\Psi_0^{(\pm)}(r) = \Phi_0^{(r)}(r) \mathcal{J}_0^{(\pm)-1}. \quad (82)$$

Since Eq.(80) is the Lippmann-Schwinger equation, it is proved that the RPA Green function is given by Eq.(35).

[1] G. C. Baldwin and G. S. Klaiber, Phys. Rev. **71**, 3 (1947).
[2] B. L. Berman and S. C. Fultz, Rev. Mod. Phys. **47**, 713 (1975).
[3] M. N. Harakeh and A. van der Woude, *Giant resonances, Fun-*

damental High-frequency modes of nuclear excitation(Oxford University Press Inc., New York, 2001).
[4] P.F. Bortignon, A. Bracco and R.A. Broglia, *Giant resonances,*

nuclear structure at finite temperature (Harwood Academic Publishers, 1998).

- [5] D. Bohm and D. Pines, Phys.Rev. **92** 609 (1953).
- [6] K.F. Liu and N. Van Giai, Phys.Lett. **65B** 23 (1976).
- [7] P. Ring and J. Speth, Nucl. Phys. **A235** 315 (1974).
- [8] P. Ring and P. Schuck, *The nuclear many body problem* (Springer, 1980).
- [9] S. Shlomo and G. Bertsch, Nucl. Phys. **A243**, 507 (1975).
- [10] *Electric and Magnetic Giant Resonances in Nuclei*, edited by J. Speth (World Scientific, Singapore, 1991).
- [11] N. Auerbach and A. Yeverchayahu, Ann. Phys. **95**, 35-52 (1975).
- [12] R. Jost and A. Pais, Phys. Rev. **82**, 840 (1951).
- [13] K. Mizuyama, N. Nhu Le, T. Dieu Thuy, and T. V. Nhan Hao, Phys. Rev. C **99**, 054607 (2019).
- [14] K. Mizuyama, N. Nhu Le, and T. V. Nhan Hao, Phys. Rev. C **101**, 034601 (2020).
- [15] K. Mizuyama, H. Cong Quang, T. Dieu Thuy, and T. V. Nhan Hao, Phys. Rev. C **104**, 034606 (2021).
- [16] S. Aoyama, T. Myo, K. Kato and K. Ikeda, Prog. Theor. Phys, **116**, 1 (2006).
- [17] T. Berggren, Nucl. Phys. **A109** (1968), 265.
- [18] R. G. Newton, J. Math. Phys. **1** (1960), 319.
- [19] H. Sagawa, Prog. Theor. Phys. Suppl. **142**, 1 (2001).
- [20] J. Terasaki, J. Engel, M. Bender, J. Dobaczewski, W. Nazarewicz, and M. Stoitsov, Phys. Rev. C **71**, 034310 (2005).
- [21] G. Col'ò, P. F. Bortignon, S. Fracasso, and N. Van Giai, Nucl. Phys. **A788**, 173c (2007).
- [22] D. Vautherin and D. M. Brink, Phys.Rev. C **5**, 626 (1972).
- [23] M. Beiner, H. Flocard, N. Van Giai, and P. Quentin, Nucl. Phys. **A238**,29(1975).
- [24] N. Van Giai, and H. Sagawa, Phys. Lett. **106B**, 379 (1981).
- [25] J. Bartel, P. Quentin, M. Brack, C. Guet, and H. B. Hakanson, Nucl. Phys. **A386**, 79 (1982).
- [26] J. Dobaczewski, H. Flocard, and J. Treiner, Nucl. Phys. **A422**, 103 (1984).
- [27] E. Chabanst, P. Bonche, P. Haensel, J. Meyer, and F. Shaeffer, Nucl. Phys. **A635**, 231 (1998).
- [28] P. G. Reinhard, D. J. Dean, et al., Phys. Rev. C **60**, 014316 (1999).
- [29] T. Sil, S. Shlomo, B. K. Agrawal, and P.-G. Reinhard, Phys. Rev. C **73**, 034316 (2006).
- [30] J.-P. Blaizot and G. Ripka, Quantum Theory of Finite Systems (The MIT Press, Cambridge, 1986).
- [31] A. M. Lane and J. Martorell, Ann. Phys. **129**, 273 (1980).
- [32] T. Nakatsukasa, T. Inakura and K. Yabana, Phys. Rev. C **76**,024318 (2007).
- [33] K. Mizuyama, G. Colo, Phys. Rev. C **85**, 024307, 2012.